2021 IEEE International Conference on Wireless for Space and Extreme Environments (WiSEE) | 978-1-6654-0371-9/21/$31.00 ©2021 IEEE | DOI: 10.1109/WiSEE50203.2021.9613835

Probabilistic Short-wave Fadeout Detection in SuperDARN Time Series Observations

Shibaji Chakraborty*, Joseph B. H. Baker† and J. Michael Ruohoniemi‡
Center for Space Science and Engineering Research
Bradley Department of Electrical and Computer Engineering
Virginia Tech, Blacksburg, USA
Email: *shibaji7@vt.edu, †bakerjb@vt.edu, ‡mikeruo@vt.edu

Abstract—**Short-wave fadeout (SWF) is one of the first space weather effects to occur in the ionosphere following a solar flare and leads to severe disruption of ionospheric HF systems. The disruption is produced by flare-enhanced energetic radiations that penetrate to the D-layer where they enhance ionization that leads to heavy absorption of high-frequency (HF, 3-30 MHz) radio signal over much of the dayside for an hour or more. In this paper, we describe two probabilistic anomaly detection schemes that have been used to detect SWF events produced by M and X class flares in Super Dual Auroral Radar Network (SuperDARN) observations. The two schemes are based on statistical Z-score and nonlinear energy operators. Performance of the detection schemes varies with flare intensity and parameters of the detection schemes. We find a correlation coefficient ∼0.73 between flare counts per month and SWF counts per month detected using the Z-score scheme.**

Index Terms—**probabilistic anomaly detection, shortwave fadeout, solar flares, HF absorption, HF propagation, ionosphere**

I. INTRODUCTION

A solar flare is a sudden intensification of the Sun's electromagnetic radiation, specifically in the EUV and X-ray wavebands of the solar spectrum, that lasts for a few tens of minutes to several hours [1]–[3]. Solar flares can be classified into five different classes in the X-ray range following the GOES classification, namely, A, B, C, M, and X with each successive class being an order of magnitude more intense than the previous class. The intensification of solar radiation during a solar flare enhances the electron density via photoionization in the dayside of the Earth's lower ionosphere (D and lower E region, ∼60-105 km) [4]. This produces an increase in ionospheric high-frequency (HF, 3-30 MHz) radio wave absorption that disrupts over-the-horizon (OTH) communication, commonly known as the Dellinger effect or Short-wave Fadeout (SWF) [5]. Previous statistical studies have shown there is almost a one-to-one correspondence between an earthward-directed solar flare and the occurrence of SWF [6]. SWF events can have serious impacts on sensitive HF systems including ground-to-ground radio communications, amateur radio links, satellite communication systems, and Global Navigation Satellite Systems [7], [8]. A recent study found solar flare-driven SWF impacts seriously degraded emergency HF communications supporting humanitarian aid services and relief efforts in the Caribbean after Hurricane Irma [9].

More recent studies have found a functional dependence of HF absorption on solar flare intensity, location of the transmitter and receiver, and frequency of the radio wave [10]–[13]. A study by Stonehocker [14] laid a foundation for nowcasting solar flare-driven HF absorption and culminated in the development of the DRAP (D Region Absorption Prediction) model currently operational at the NOAA (National Oceanic and Atmospheric Administration) SWPC (Space Weather Prediction Center) [15]. Such a predictive capability is useful but radio operators also need to be able to monitor, in near real-time (NRT), the occurrence, extent, and intensity of an ongoing event. We propose to use SuperDARN (Super Dual Auroral Radio Network) observations to develop such a monitoring network across North America. The SuperDARN HF radar technique possesses distinct advantages in that it operates in the range of frequencies that is of most interest to radio operators, is more sensitive to absorption effects due to its relatively low frequency, and sees effects of solar flares that precede SWF.

We have developed a SWF detection capability based on spike detection in historical observations from SuperDARN radars located in North America and compiled a list of SWF events detected during 2011-2015. This SWF detection capability is a first step toward developing a NRT monitoring system based on SuperDARN observations. Here, we describe two algorithmic formulations of SWF detection and report on their accuracy.

The paper is organized as follows: Section II provides a brief introduction to instruments and datasets used in the study; Section III describes two spike detection schemes; Section IV presents results demonstrating the accuracy of the schemes; and Section V summarizes our findings.

II. DATA SOURCES

The primary datasets used in this study are solar flare intensity measurements and HF backscatter echoes from the GOES X-ray sensors and SuperDARN HF radars, respectively.

Solar X-ray flux information was obtained from the National Oceanic and Atmospheric Administration (NOAA) GOES 15 satellite [16]. The solar X-ray sensors on GOES 15 satellites have two channels, namely hard X-ray (0.05-0.4 nm,

This study is funded by NASA SWO2R-80NSSC20K1380.

HXR) and soft X-ray (0.1-0.8 nm, SXR). The NOAA archive supports high resolution (2 seconds) and low resolution (1 minute averaged over high resolution) X-ray data. The solar flux information from both X-ray channels is used as a solar flare reference.

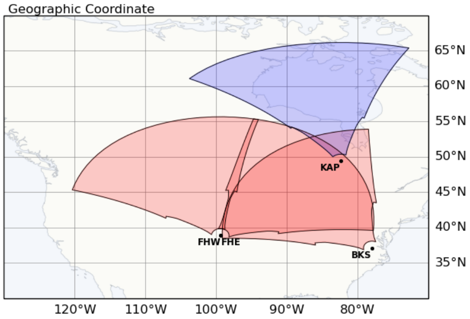

Fig. 1. Field-of-view (FoV) of the SuperDARN radars, located at middle (in red) and high (in blue) latitudes, used in this study.

TABLE I
SUPERDARN RADAR LOCATION DETAILS.

Radar Names	Radar Codes	Geographic Coordinates	
		Latitudes	*Longitudes*
Blackstone	BKS	37.10	-77.95
Fort Hays East	FHE	38.86	-99.39
Fort Hays West	FHW	38.86	-99.39
Kapuskasing	KAP	49.39	-82.32

SuperDARN is a network of HF radars, operating between 8 and 18 MHz, distributed across the middle, high, and polar latitudes of both hemispheres. Each radar measures backscatter from decameter-scale ionospheric plasma irregularities (ionospheric scatter) and the Earth's surface (ground scatter) [17]–[19]. The field-of-view (FoV) typically comprises 16 to 20 azimuth beams spanning a sector $\sim 50^o$ in width and 75-110 range gates spaced 45 km apart starting at 180 km range. The typical integration time of each beam sounding is 3 or 6 seconds, which results in a full radar sweep through all beams in 1 or 2 minutes. Figure 1 shows the locations and fields-of-view of the SuperDARN radars used in this study while Table I lists their positions in geographic coordinates.

Figure 2 presents Blackstone (BKS) radar measurements and GOES X-ray fluxes on 11 March 2015. Panel (a) shows there were two prominent flares on that day: an X2.2 class event with peak intensity at 16:22 UT followed by an M1.0 class event that peaked at 18:50 UT. The X2.2 event initiated at 16:10 UT when the GOES X-ray sensor observed a sudden increase in solar X-ray flux (panel a). In response, BKS observed a decrease in the number of backscatter echoes (panel b) leading to a total blackout of the radio link in about 10 minutes followed by a gradual recovery over $\sim$ 30-60 minutes. The M1.0 event had a compound initiation with a small C-class onset starting at $\sim$18:40 UT followed by a larger M-class onset at $\sim$18:45 UT. There is some evidence of a decrease in BKS backscatter echoes but the response in this case is weak. It can be seen that the signature of an SWF commencement following an X-class flare is an inverted spike in the number of backscatter observations, while the effects of M-class flare are more gradual and weaker. These facts are also reported in our previous studies [10], [12].

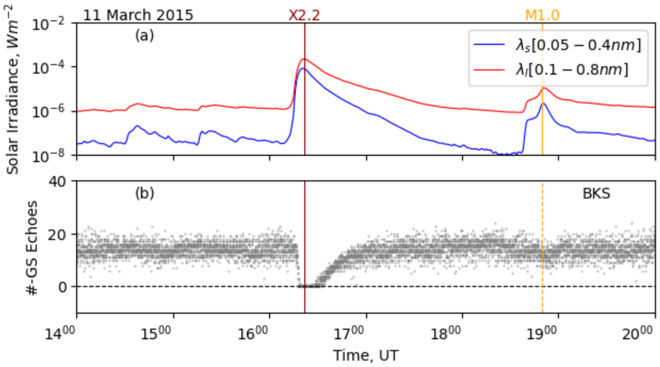

Fig. 2. GOES and Blackstone (BKS) radar measurements during a solar flare and associated SWF event on 11 March 2015: (a) GOES X-ray flux in the 0.1–0.8 nm (red) and 0.05–0.4 nm (blue) wavelength bands and (b) number of BKS backscatter echoes. The vertical lines passing through both panels identify the peak times of X2.2 (red) and M1.0 (orange) class events.

III. DETECTION SCHEMES

In this study we have used two different spike detection techniques to identify SWF signatures in SuperDARN backscatter observations. First, a modified Z-score based spike detection technique, also referred as the Whitaker-Hayes algorithm [20], and second, a nonlinear energy operator (NEO) [21].

A. Modified Z-score

Z-score represents how many standard deviations away a given observation is from the mean. By contrast, the modified Z-score is estimated using the median (M) and median absolute deviation (MAD) instead of mean and standard deviation. Equation 1 presents the modified Z-score assuming the backscatter count (e_n) is normally distributed. The multiplier 0.6745 in the equation is the 0.75^{th} quartile of the standard normal distribution, to which the MAD converges:

$$z(e_n) = 0.6745 \times \frac{e_n - e_n^M}{e_n^{MAD}} \tag{1}$$

where: e_n^M, e_n^{MAD}, and $z(e_n)$ are the median, median absolute deviations, and Z-score of backscatter count (e_n). For a spike the $z(e_n)$ value is high.

B. Nonlinear Energy Operator

The NEO provides a measure of change in the instantaneous energy (i.e., squared magnitude of the considered signal) in the signal, here SuperDARN radar backscatter count (e_n) [22]. Previous studies have found that NEO can discriminate between spikes and noise better than a simple thresholding detector, specifically when the signal-to-noise ratio (SNR) is low [22]. Another study found the NEO provided more accurate spike detection than detectors and had lower computational requirements [21]. The main goal of the NEO, defined in Equation 2, is to emphasize the difference between spikes and noise. The NEO adapts to changes in SNR level to identify the spike in the data:

$$neo(e_n) = \dot{e}_n^2 - \ddot{e}_n e_n \tag{2}$$

where: $\dot{e}_n$, $\ddot{e}_n$, and $neo(e_n)$ are the first, second order time derivative, and spike score of backscatter count (e_n) estimated using the NEO. For a spike the value of $neo(e_n)$ is high.

C. Probabilistic Detection Schemes

Algorithm 1 outlines the steps of a pseudo code to detect spikes observed in daytime SuperDARN backscatter observations following flare driven SWFs. The algorithm applies a time window to the radar data obtained on each beam and calculates a spike score using both of the operators described in the two previous subsections. The difference between the spike score and a spike threshold is projected onto a sigmoid curve to estimate probability. The algorithm then estimates median spike probability $\mu^{(x)}$ across the beams, multiple beam detection probability $\theta^{(x)}$, and reliability score $\gamma^{(x)}$ for all beams during that time window. The detection probability $\tau^{(x)}$ is estimated by multiplying $\mu^{(x)}$ and $\theta^{(x)}$. More details about these metrics are listed in Table II. The final output is the probability and reliability score, both of which need to be high for a successful spike detection.

Algorithm 1: Pseudo code for SWF detection in SuperDARN backscatter observations.

```
Input: data ($D$), window length ($\Delta T$), threshold ($s_{th}$)
Result: $\tau_s$, $\gamma_s$
initialization $\rightarrow$B=total radar beams, $\gamma_s = [], \tau_s = []$;
while data chunk available in $D$ do
    remove data with solar zenith angle ($\chi$) $\geq 90^o$;
    take data chunk $d_c$ with window length = $\Delta T$;
    initialization $\rightarrow \beta = 0, p = []$;
    for each beam (b) in radar do
        run Z-score OR NEO on $d_c$;
        threshold score ($s$) based on $s_{th}$;
        if $s \geq s_{th}$ then
            increment $\beta$ by one;
        end
        estimate probability $pr = \frac{1}{1+e^{-(s-s_{th})}}$;
        add $pr$ to $p$ list;
    end
    estimate the following parameters for $\Delta T$ window;
    $\mu^{(x)} = M(p)$, $\theta^{(x)} = \frac{\beta}{B}$;
    $\tau^{(x)} = \mu^{(x)} \times \theta^{(x)}$, and $\gamma^{(x)} = -10log[MAD(p)]$;
    add $\gamma^{(x)}$ and $\tau^{(x)}$ to $\gamma_s$ and $\tau_s$ lists;
end
```

TABLE II
SIGNIFICANCE OF METRICS USED IN THE DETECTION SCHEME.

Symbol	Description	Range
$\mu^{(x)}$	Median spike probability across the beams: Probability that a spike occurred.	[0-1]
$\theta^{(x)}$	Beam detection probability: Probability that a spike occurred across multiple beams within ΔT interval.	[0-1]
$\tau^{(x)}$	Probability that a spike occurred: Probability that a spike occurred across different beams within ΔT interval, a high value is preferred for good detection.	[0-1]
$\gamma^{(x)}$	Reliability score: Quantify uncertainty in $\tau^{(x)}$ estimates. A high value is expected for a reliable $\tau^{(x)}$ estimate.	[0-∞)

$^{(x)}$ is replaced with z or n based on the spike detectors, i.e., Z-scores or NEO, respectively.

IV. RESULTS

In this section, we present some example outputs from application of the spike detection algorithm. First, we present a classic example of shortwave fadeout observed in BKS backscatter and the outputs from application of the algorithm. Then, we presents statistical results showing how the performance of the algorithm varies with solar flare intensity and window length.

A. Event Analysis: 11 March 2015

Figure 3 presents example results from the SWF detection scheme applied to BKS radar data obtained on 11 March, 2015. For this case, the algorithm used a time window (ΔT) of 2 hours and spike thresholds (s_{th}) of -3 and 15 for the Z-score and NEO operators, respectively. From top to bottom the panels show the number of backscatter echoes, spike scores, median probabilities $\mu^{(x)}$, detection probabilities $\tau^{(x)}$, and reliability scores.

It can be seen that both spike operators successfully detect the SWF signature in the BKS data created by the X-class flare but neither identifies a SWF signature for the compound M-class flare. Also, the probability estimated using the Z-score is significantly higher for all three 2-hour window intervals.

Table III lists the spike detection probability and reliability scores for the X and M-class flares using data from the BKS, FHE, and KAP radars for the 6-hour window identified in Figure 3. For the X-class flare, both operators have detected spikes with high probabilities ($\tau^{(x)} \geq 0.9$) and reliability scores ($\gamma^{(x)} \geq 8$). For the M-class flare Z-score based operator is able to detect the spike with moderate probabilities ($\tau^{(x)} \sim 0.5$) and high reliability scores ($\gamma^{(x)} \geq 8$), but the NEO estimates no spike with low probabilities ($\tau^{(x)} \sim 0.01$) with high reliability scores. This shows, among both operators the NEO is conservative in nature.

B. Statistical Analysis

Figure 4 compares the monthly count of M and X-class flares observed by GOES spacecraft with the mean number of SWF spikes detected by the algorithm in data collected by the four radars over half a decade. The algorithm was run using

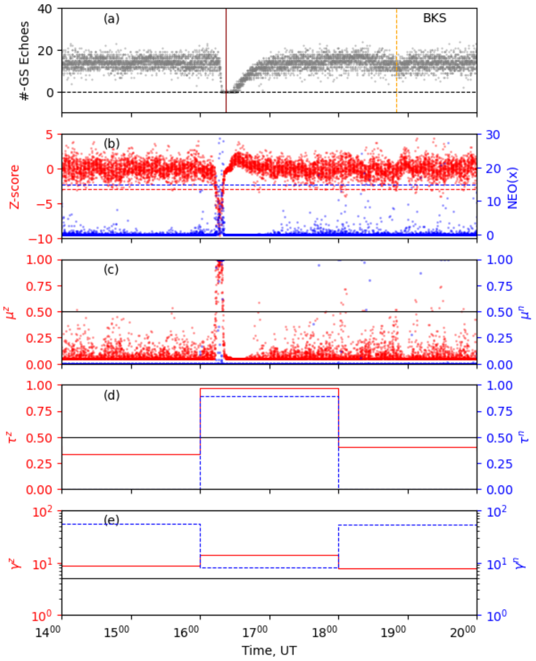

Fig. 3. Results from the SWF detection scheme applied to BKS radar data obtained on 11 March, 2015: (a) number of BKS backscatter echoes, (b) spike scores, (c) median probabilities, (d) detection probabilities within 2-hour window, and (e) reliability scores. Red and blue colors represent outputs from the Z-score and NEO operators, respectively. Red and blue horizontal lines in panel (b) represent threshold scores s_{th} for the Z-score and NEO, respectively. Horizontal black lines passing through panels (c-d) represent threshold of detection probability 0.5, while the same for panel (e) represents threshold of detection certainty 5.

TABLE III
SPIKE DETECTION PARAMETERS FOR THE FLARES ON 11 MARCH 2015.

Radar	Flare X2.2	Flare M1
BKS	$\tau^n = 0.9, \gamma^n = 8$	$\tau^n = 0, \gamma^n = 52$
	$\tau^z = .96, \gamma^z = 14.2$	$\tau^z = 0.4, \gamma^z = 7$
FHE	$\tau^n = 1, \gamma^n = \infty$	$\tau^n = 0, \gamma^n = 44$
	$\tau^z = 0.96, \gamma^z = 12.2$	$\tau^z = 0.5, \gamma^z = 7$
KAP	$\tau^n = 1, \gamma^n = 75$	$\tau^n = 0.01, \gamma^z = 41.3$
	$\tau^z = 0.81, \gamma^z = 10$	$\tau^z = 0.6, \gamma^z = 71.3$

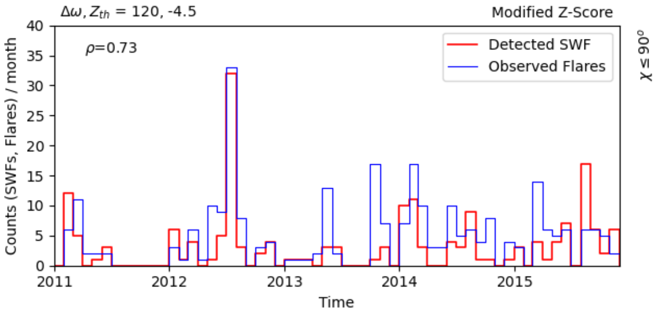

Fig. 4. Monthly count of M and X-class flares observed by GOES spacecraft (blue) and SWF signatures (red) detected in data collected by the BKS, FHE, FHW and KAP radars for five years (2011-2015). The algorithm was run using the modified Z-score operator with a time window $\Delta T = 120$ minutes and a threshold Z-score Z_{th}=-4.5. The correlation coefficient between the two time series is $\rho = 0.73$.

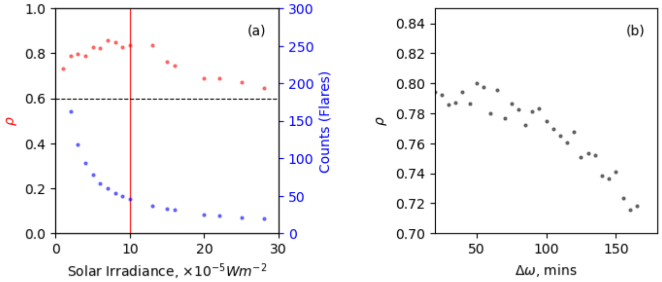

Fig. 5. Variation of the solar flare - SWF spike correlation coefficient versus (a) solar flare irradiance, and (b) length of time window. Blue and red dots in panel (a) represent the number of flares and the correlation coefficient, respectively. The vertical red line in panel (a) corresponds to an X1-class flare. Correlation coefficients in panel (a) were calculated using a fixed time window ΔT= 120 minutes while those in panel (b) include all flares of intensity M2 class and higher. All other algorithmic parameters are the same as described in Figure 3.

the modified Z-score operator, a 2-hour time window, and a threshold Z-score of -4.5. The mean SWF count is rounded off to the nearest whole number. The correlation coefficient between these two time series data is 0.73, which indicates that the algorithm performs reasonably well extracting flare-driven SWF spikes from the historical SuperDARN archive.

Figure 5 shows how the solar flare - SWF spike correlation coefficient varies with (a) minimum threshold of solar flare irradiance and (b) the length of the time window. The correlation coefficients in (a) were calculated using a fixed 2-hour time window while those in (b) used a fixed lower flare intensity threshold corresponding to M2 class. All other algorithmic parameters correspond to the same values used to generate Figure 3. Panel (a) shows the correlation coefficient maximizes near a minimum flare intensity threshold corresponding to X1 class (red vertical line). Below this threshold, the correlation is lower because of the weaker SWF response to M-class flares seen in Figure 2, while above the X1 threshold the correlation becomes increasingly degraded by poor statistics. Panel (b) shows the correlation coefficient steadily decreases as the length of the time window is increased, with a much sharper rate of decrease beyond an hour or so. When the time window is too long, it is difficult to identify the SWF spikes against the background of hour-to-hour diurnal variations.

V. CONCLUSIONS & APPLICATIONS

This paper presents a probabilistic method for solar flare-driven SWF spike detection in SuperDARN HF backscatter observations. The scheme utilizes statistical Z-score and non-linear energy operator (NEO) based spike detection techniques to identify sudden reductions in the number of SuperDARN backscatter echoes produced by SWF. We found the Z-score method outperforms the NEO method, particularly for weaker M-class flares. A correlation analysis of monthly solar flare count versus SWF spike detection demonstrates the algorithm performs reasonably well identifying SWF signatures in the historical SuperDARN archive, particularly for X1-class flares and higher. The correlation was also found to decrease substantially when the time window for spike detection is longer than an hour or so. Future work includes: (1) creating a list of SWF events in the SuperDARN historical archive for wider scientific community use, and (2) developing a near real-time monitoring system for tracking the occurrence, extent, and intensity of ongoing SWF events for radio system operators.

ACKNOWLEDGMENT

The authors thank to NASA for support this study under grant SWO2R-80NSSC20K1380. The operations of BKS, KAP, FHE, and FHW SuperDARN radar is supported under NSF award AGS-193110. The authors also wish to acknowledge the use of the NOAA/GOES X-ray data for flare confirmation and analysis. We thank all participants in the worldwide SuperDARN collaboration for the distribution of SuperDARN data via this URL. Lastly, the authors acknowledge Advanced Research Computing at Virginia Tech for providing computational resources and technical support that have contributed to the results reported within this paper. The majority of analysis and visualization was completed with the help of free, open-source software tools such as matplotlib [23], IPython [24], pandas [25], PyForecastTools [26], and others [27].

REFERENCES

[1] R. Hansen and J. Kleczek, "Coincidence of Sudden Ionospheric Disturbances with the Explosive Phase of Solar Flares," Tech. Rep., 1962.

[2] R. G. Rastogi, B. M. Pathan, D. R. K. Rao, T. S. Sastry, and J. H. Sastri, "Solar Flare Effects on the Geomagnetic Elements during Normal and Counter Electrojet Periods," *Earth, Planets and Space*, vol. 51, no. 9, pp. 947–957, 9 1999. [Online]. Available: http://earth-planets-space.springeropen.com/articles/10.1186/BF03351565

[3] D. E. Siskind, K. A. Zawdie, F. Sassi, D. Drob, and M. Friedrich, "Global Modeling of the low- and middle-latitude Ionospheric D and lower E Regions and Implications for HF Radio Wave Absorption," *Space Weather*, vol. 15, no. 1, pp. 115–130, 1 2017. [Online]. Available: http://doi.wiley.com/10.1002/2016SW001546

[4] K. Davies, *Ionospheric Radio*, 1990.

[5] J. H. Dellinger, "Sudden ionospheric disturbances," *Terrestrial Magnetism and Atmospheric Electricity*, vol. 42, no. 1, pp. 49–53, 1937. [Online]. Available: https://agupubs.onlinelibrary.wiley.com/doi/abs/10.1029/TE042i001p00049

[6] H. DeMastus and M. Wood, "Short-wave fadeouts without reported flares," *Journal of Geophysical Research*, vol. 65, no. 2, pp. 609–611, 2 1960. [Online]. Available: https://agupubs.onlinelibrary.wiley.com/doi/full/10.1029/JZ065i002p00609https://agupubs.onlinelibrary.wiley.com/doi/abs/10.1029/JZ065i002p00609https://agupubs.onlinelibrary.wiley.com/doi/10.1029/JZ065i002p00609

[7] N. A. Frissell, J. S. Vega, E. Markowitz, A. J. Gerrard, W. D. Engelke, P. J. Erickson, E. S. Miller, R. C. Luetzelschwab, and J. Bortnik, "High-Frequency Communications Response to Solar Activity in September 2017 as Observed by Amateur Radio Networks," *Space Weather*, vol. 17, no. 1, pp. 118–132, 2019. [Online]. Available: https://agupubs.onlinelibrary.wiley.com/doi/abs/10.1029/2018SW002008

[8] D. J. Knipp, A. C. Ramsay, E. D. Beard, A. L. Boright, W. B. Cade, I. M. Hewins, R. H. McFadden, W. F. Denig, L. M. Kilcommons, M. A. Shea, and D. F. Smart, "The May 1967 great storm and radio disruption event: Extreme space weather and extraordinary responses," *Space Weather*, vol. 14, no. 9, pp. 614–633, 9 2016. [Online]. Available: https://agupubs.onlinelibrary.wiley.com/doi/abs/10.1002/2016SW001423http://doi.wiley.com/10.1002/2016SW001423

[9] R. J. Redmon, D. B. Seaton, R. Steenburgh, J. He, and J. V. Rodriguez, "September 2017's Geoeffective Space Weather and Impacts to Caribbean Radio Communications During Hurricane Response," *Space Weather*, vol. 16, no. 9, pp. 1190–1201, 9 2018. [Online]. Available: http://doi.wiley.com/10.1029/2018SW001897

[10] S. Chakraborty, J. M. Ruohoniemi, J. B. H. Baker, and N. Nishitani, "Characterization of Short-Wave Fadeout Seen in Daytime SuperDARN Ground Scatter Observations," *Radio Science*, vol. 53, no. 4, pp. 472–484, 2018. [Online]. Available: https://agupubs.onlinelibrary.wiley.com/doi/abs/10.1002/2017RS006488

[11] S. Chakraborty, J. B. H. Baker, J. M. Ruohoniemi, B. Kunduri, N. Nishitani, and S. G. Shepherd, "A Study of SuperDARN Response to Co-occurring Space Weather Phenomena," *Space Weather*, vol. 17, no. 9, pp. 1351–1363, 2019. [Online]. Available: https://agupubs.onlinelibrary.wiley.com/doi/abs/10.1029/2019SW002179

[12] R. A. D. Fiori, A. V. Koustov, S. Chakraborty, J. M. Ruohoniemi, D. W. Danskin, D. H. Boteler, and S. G. Shepherd, "Examining the Potential of the Super Dual Auroral Radar Network for Monitoring the Space Weather Impact of Solar X-Ray Flares," *Space Weather*, vol. 16, no. 9, pp. 1348–1362, 9 2018. [Online]. Available: http://doi.wiley.com/10.1029/2018SW001905

[13] D. Watanabe and N. Nishitani, "Study of Ionospheric Disturbances During Solar Flare Events Using the SuperDARN Hokkaido Radar," *Advances in Polar Science*, vol. 24, no. 1, pp. 12–18, 2013.

[14] G. H. Stonehocker, "Advanced telecommunication forecasting technique in AGY." 5th. Ionospheric forecasting, AGARD, 1970, pp. 27–31.

[15] H. H. Sauer and D. C. Wilkinson, "Global mapping of ionospheric HF/VHF radio wave absorption due to solar energetic protons," *Space Weather*, vol. 6, no. 12, 12 2008. [Online]. Available: http://doi.wiley.com/10.1029/2008SW000399

[16] J. Machol, "GOES X-ray Sensor (XRS) Measurements Important notes for users," Tech. Rep., 2016.

[17] G. Chisham, M. Lester, S. E. Milan, M. P. Freeman, W. A. Bristow, A. Grocott, K. A. McWilliams, J. M. Ruohoniemi, T. K. Yeoman, P. L. Dyson, R. A. Greenwald, T. Kikuchi, M. Pinnock, J. P. S. Rash, N. Sato, G. J. Sofko, J.-P. Villain, and A. D. M. Walker, "A decade of the Super Dual Auroral Radar Network (SuperDARN): scientific achievements, new techniques and future directions," vol. 28, no. 1, pp. 33–109, 2007. [Online]. Available: https://doi.org/10.1007/s10712-007-9017-8

[18] R. A. Greenwald, K. B. Baker, R. A. Hutchins, and C. Hanuise, "An HF phased-array radar for studying small-scale structure in the high-latitude ionosphere," *Radio Science*, vol. 20, no. 1, pp. 63–79, 1985. [Online]. Available: https://agupubs.onlinelibrary.wiley.com/doi/abs/10.1029/RS020i001p00063

[19] N. Nishitani, J. M. Ruohoniemi, M. Lester, J. B. H. Baker, A. V. Koustov, S. G. Shepherd, G. Chisham, T. Hori, E. G. Thomas, R. A. Makarevich, A. Marchaudon, P. Ponomarenko, J. A. Wild, S. E. Milan, W. A. Bristow, J. Devlin, E. Miller, R. A. Greenwald, T. Ogawa, and T. Kikuchi, "Review of the accomplishments of mid-latitude Super Dual Auroral Radar Network (SuperDARN) HF radars," vol. 6, no. 1, p. 27, 2019. [Online]. Available: https://doi.org/10.1186/s40645-019-0270-5

[20] D. Whitaker and K. Hayes, "A simple algorithm for despiking raman spectra," *ChemRxiv*, 2018.

[21] S. Mukhopadhyay and G. Ray, "A new interpretation of nonlinear energy operator and its efficacy in spike detection," *IEEE Transactions on Biomedical Engineering*, vol. 45, no. 2, pp. 180–187, 1998.

[22] K. H. Kim and S. J. Kim, "Neural spike sorting under nearly 0-db signal-to-noise ratio using nonlinear energy operator and artificial neural-network classifier," *IEEE Transactions on Biomedical Engineering*, vol. 47, no. 10, pp. 1406–1411, 2000.

[23] J. D. Hunter, "Matplotlib: A 2D graphics environment," *Computing In Science & Engineering*, vol. 9, no. 3, pp. 90–95, 2007. [Online]. Available: https://ieeexplore.ieee.org/document/4160265

[24] F. Perez and B. E. Granger, "Ipython: A system for interactive scientific computing," *Computing in Science Engineering*, vol. 9, no. 3, pp. 21–29, May 2007. [Online]. Available: https://ieeexplore.ieee.org/document/4160251

[25] W. McKinney, "Data Structures for Statistical Computing in Python," in *Proceedings of the 9th Python in Science Conference*, S. van der Walt and J. Millman, Eds., 2010, pp. 56–61. [Online]. Available: https://conference.scipy.org/proceedings/scipy2010/mckinney.html

[26] S. Morley, "drsteve/PyForecastTools: PyForecastTools," Jun. 2018. [Online]. Available: https://doi.org/10.5281/zenodo.1256921

[27] K. J. Millman and M. Aivazis, “Python for Scientists and Engineers,” *Computing in Science & Engineering*, vol. 13, no. 2, pp. 9–12, 2011. [Online]. Available: https://ieeexplore.ieee.org/document/5725235